N-doped Mesoporous Titania as a Photoelectrochemical Working Electrode for Dye-Sensitized Solar Cells

Shou-Heng Liu[*] *, Jhe-Wei Syu*

Department of Chemical and Materials Engineering, National Kaohsiung University of Applied Sciences, Kaohsiung 80778, Taiwan
*E-mail: shliu@kuas.edu.tw

Nanocrystalline titania (Non-Meso TiO_2), mesoporous titania (Meso TiO_2) and nitrogen-doped mesoporous titania (N-doped Meso TiO_2) were synthesized via a simple evaporation induced self-assembly (EISA) process. The obtained materials were thoroughly characterized by various spectroscopic and analytical techniques, including small-angle X-ray scattering (SAXS), X-ray diffraction (XRD), transmission electron microscopy (TEM), UV-visible and X-ray photoelectron spectroscopies (XPS) analysis. Among all prepared photoanodes for dye-sensitized solar cells (DSSCs), the N-doped Meso TiO_2 photoanodes showed the maximum conversion efficiency with an open circuit voltage (*Voc*) of 0.75 V, a short circuit density (*Jsc*) of 11.07 mA cm^{-2}, a fill factor (*FF*) of 63%, and an efficiency of 5.3%. This may be attributed to the formation of O-Ti-N linkage in the N-doped Meso TiO_2 electrode, retarding the recombination reaction at the interface of TiO_2 photoelectrode and electrolyte as compared to the Non-Meso TiO_2 and Meso TiO_2 DSSCs.

Keywords: Mesoporous titania, N-doping, Dye-sensitized solar cells, Photoelectrochemistry.

1. INTRODUCTION

Dye-sensitized solar cells (DSSCs) have been considered as one of the next-generation power sources due to their advantages of low-cost and high-efficiency solar energy conversion [1-9]. The dye sensitizers are photoexcited and sequentially fast injection of electrons into the TiO_2 conduction band is happened during operation. However, the injected electrons of conduction band may recombine with oxidized dye molecules or react with redox species in electrolyte, resulting in decreasing overall conversion efficiency. To unravel this problem, various methods have been investigated for retarding the charge recombination of DSSCs, such as the utilization of novel dyes [10,11], core-shell nanomaterials [12-14], and doping nonmetal [15-19]. Among the nonmetal doping systems, N-doping has been demonstrated to be a good candidate due to its unique properties of high thermal stability,

low carrier-recombination centers [20,21] and perfecting the oxygen deficiency and decreasing the back reaction mentioned above. Since the study by Asahi et al. in 2001 [22], many methods have been reported to prepare N-doping of TiO_2, such as thermal oxidation, anodization, sputtering and ion implantation methods [23-25]. Nonetheless, these methods need to be performed under relatively severe conditions and hence hinder the large-scale implementation.

Mesoporous materials, which possess hierarchical and tunable pore architecture, have received enormous interest because of their potential applications in many fields such as catalysis, energy storage and conversion, and separation technology [26-34]. Among them, mesoporous TiO_2 with high specific surface area can facilitate a high degree of photosensitive dye loading as well as an efficient light harvesting. Therefore, a variety of potential applications in photocatalytic and photovoltaic applications was widely found in the recent years [35-40]. Generally, most of the approaches for the preparation of mesoporous TiO_2 use soft-templating and hard-templating routes [41,42]. Even though above-mentioned methods are well established for preparing mesoporous TiO_2, the synthesis routes invoked in those materials were still restricted by the ineffectiveness in material cost and preparation time, which further hinder their industrial applications. Furthermore, the synthesis of TiO_2 by integrating mesoporosity and N-doping via a simple route is very scarce.

In this paper, a facile procedure to fabricate nanocrystalline titania (denoted as Non-Meso TiO_2), mesoporous titania (denoted as Meso TiO_2) and N-doped mesoporous TiO_2 (denoted as N-doped Meso TiO_2) by using evaporation induced self-assembly (EISA) approach was reported. The nanomaterials so fabricated were found to possess N-doped and mesoporous structural TiO_2 which had superior photovoltaic properties, rendering potential applications in solar-energy related areas, for example, as photoanodes for DSSCs.

2. EXPERIMENTAL

For preparation of titania without mesoporosity (denoted as Non-Meso TiO_2), ca. 2 g pluronic F127 tri-block copolymer ($EO_{106}PO_{70}EO_{106}$, MW = 12600, Sigma-Aldrich) was dissolved in a mixture solution containing 40 mL of absolute ethanol with 3.3 g (35 wt%) of hydrochloric acid by constantly stirring. Then, 1.3 g of citric acid was added in 4 mL water and then introduced into the above solution under vigorous stirring for 2 h at room temperature. About 5.7 g titanium (IV) isopropoxide (Acros) and x g of urea ($x = 0$) dissolved in y mL ($y = 160$) of absolute ethanol was added slowly to the above solution. The mixture solution was stirred at 343 K for 2 days to obtain the solid product by the evaporation induced self-assembly (EISA) technique. Finally, the sample was increased the temperature to 773 K with a heating rate of 1 K min^{-1} and eventually maintained at the same temperature for 5 h in the presence of air to remove template. Similar procedures were adopted for the syntheses of titania with mesoporosity (denoted as Meso TiO_2), except that the absolute ethanol (y) was added with 40 mL during EISA process. For preparation of N-doped mesoporous titania (denoted as N-doped Meso TiO_2), a similar procedure was also carried out except that x and y values mentioned above were 2.5 and 40, respectively.

The mesostructure of samples was investigated by small-angle X-ray scattering (SAXS) using a Nanostar U system (Bruker, AXS Gmbh). The crystalline properties of all samples were analyzed by large-angle X-ray diffraction (XRD) with a PANalytical (X'Pert PRO) instrument using Cu-Kα radiation ($\lambda = 0.1541$ nm). Nitrogen adsorption-desorption isotherms were measured at 77 K on a Micromeritics ASAP 2020 analyzer. The Brunauer-Emmett-Teller (BET) approach was used to evaluate specific surface area from nitrogen adsorption data in the relative pressure (P/P_0) range from 0.05 to 0.2. Pore size distribution curves were analyzed by the BJH method from the adsorption branch. The total pore volume was estimated from the amount adsorbed at the P/P_0 of 0.99. The high-resolution transmission electron microscopy (TEM) was done at room temperature using an electron microscope (JEOL TEM-3010) operating at an electron acceleration voltage of 200 kV. The electronic structure and N-doping amount of samples were determined by X-ray photoelectron spectra (XPS) which obtained on a spectrometer (Kratos Axis Ultra DLD) with a constant pass energy of 20 eV followed by irradiating a sample pellet (6mm in diameter) with amonochromatic Al-Ka (1486.6 eV) X-ray under ultra-high vacuum condition (10^{-10} Torr). Absorbance spectra of samples were recorded in the diffuse reflectance mode using JASCO V-670 UV-visible spectrometer equipped with an integrating sphere setup.

The TiO_2 and modified TiO_2 photoanodes were prepared by doctor blading the TiO_2 paste on the glass FTO (fluorine-doped tin oxide). The adsorption of dye on the TiO_2 surface was carried out by immersing the prepared photoanodes in the ethanol solution containing N719 dye for 16 h at room temperature. The dye-coated photoanode and a Pt-coated FTO glass cathode were assembled like a sandwich via a 60 μm spacer of hot-melt thermal foil (Solaronix SA). An electrolyte containing 0.1 M of LiI (Aldrich), 0.05 M of I_2 (Riedel-de Haen), 0.6 M of DMPII (Solaronix SA), and 0.5 M of 4-tert-butylpyridine (Aldrich) in acetonitrile was then infiltrated between the two electrodes of the DSSC and sealed with AB epoxy. The photocurrent-voltage characteristics of DSSCs were measured with a Keithley model 2400 digital source meter under one-sun illumination (AM1.5, 100 mW cm^{-2}).

3. RESULTS AND DISCUSSION

Figure 1 shows the small-angle powder X-ray scattering patterns of various samples. No feature was observed for Non-Meso TiO_2 sample, indicating the lack of a long-range mesostructural ordering. However, one broad peak centering at $2\theta = \sim 0.3^\circ$ was observed for the Meso TiO_2 sample, suggesting that TiO_2 nanoparticles assembled with a well-ordered array of mesopores. However, a decrease in peak intensity of N-doped Meso TiO_2 sample due to the reduced mesoporous ordering was found upon the addition of urea during EISA, implying that presence of urea in synthetic mixture perturb the self-assembly process. The mesoporous structures of various samples are also confirmed by N_2 adsorption/desorption isotherms. Meso TiO_2 and N-doped Meso TiO_2 samples showed typical signatures for mesoporosity, namely type-IV isotherms with well-defined hysteresis loops (not shown). The textural properties of various samples including BET surface area, average pore diameter, and pore volume derived from N_2 adsorption/desorption isotherms and pore size distributions are listed in Table 1. Meso TiO_2 and N-doped Meso TiO_2 samples were found to possess higher BET surface areas

and pore volumes compared to those of Non-Meso TiO_2. This may be due to the fact that well-defined mesostructures of Meso TiO_2 and N-doped Meso TiO_2 samples were formed during the EISA process.
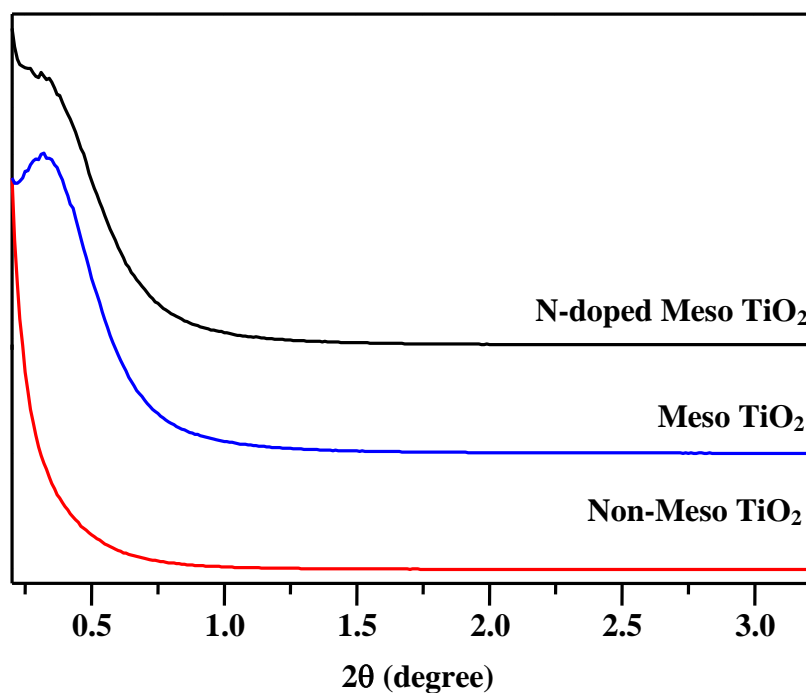

Figure 1. Small angle X-ray scattering patterns of various samples.

The large-angle XRD patterns of various samples in Figure 2 all showed well-resolved peaks characteristic of (101), (004), (200), (105), (211), (204), (116), (220) and (215) diffraction peaks at 2θ = 25.3°, 37.9°, 48.3°, 53.9°, 55.2°, 62.9°, 69.1°, 70.3° and 75.2°, respectively, indicating the well crystalline anatase phase (JCPDS, No. 21-1272) of TiO_2 in all samples. The corresponding crystallite size (d_p) was estimated by using Scherrer formula based on the (101) diffraction peak, as shown in Table 1. The obtained d_p was affected by ethanol solvents and urea. For instance, the decreased d_p observed for the N-doped Meso TiO_2 samples upon addition of urea during EISA process, indicating that the suppression of the hydrolysis in the TiO_2 colloidal solution could restrain the grain growth when urea used as a nitrogen source.

To further investigate the crystalline phase of prepared samples, a representative high-resolution TEM image of N-doped Meso TiO_2 is shown in Figure 3. Each individual nanocrystal of N-doped Meso TiO_2 consisted of well-defined lattice fringes of 0.35 nm which is in a good agreement with the (101) plane of the anatase phase of TiO_2. Also, selected area electron diffraction (SAED) of the N-doped Meso TiO_2 samples is shown in the inset of Figure 3. The obtained results confirmed that pore walls of N-doped Meso TiO_2 are nanocrystalline oxides that show well-defined diffuse electron diffraction rings which are assigned as (101), (004), (200), (211), (204), (220) and (215) in their respective SAED pattern. The sharp rings in SAED pattern suggested that the TiO_2 anatase phase possessed a high crystallinity, which is again consistent with the above-mentioned XRD result.

The change of the N-doping, chemical binding state on the TiO_2 lattice was surveyed by XPS. As can be seen in Figure 4, XPS spectra of Ti 2p core levels of various samples indicated that the spin-orbit split lines of Ti $2p_{3/2}$ and Ti $2p_{1/2}$ at ca. 459 and 465 eV, respectively, were observed in all Ti
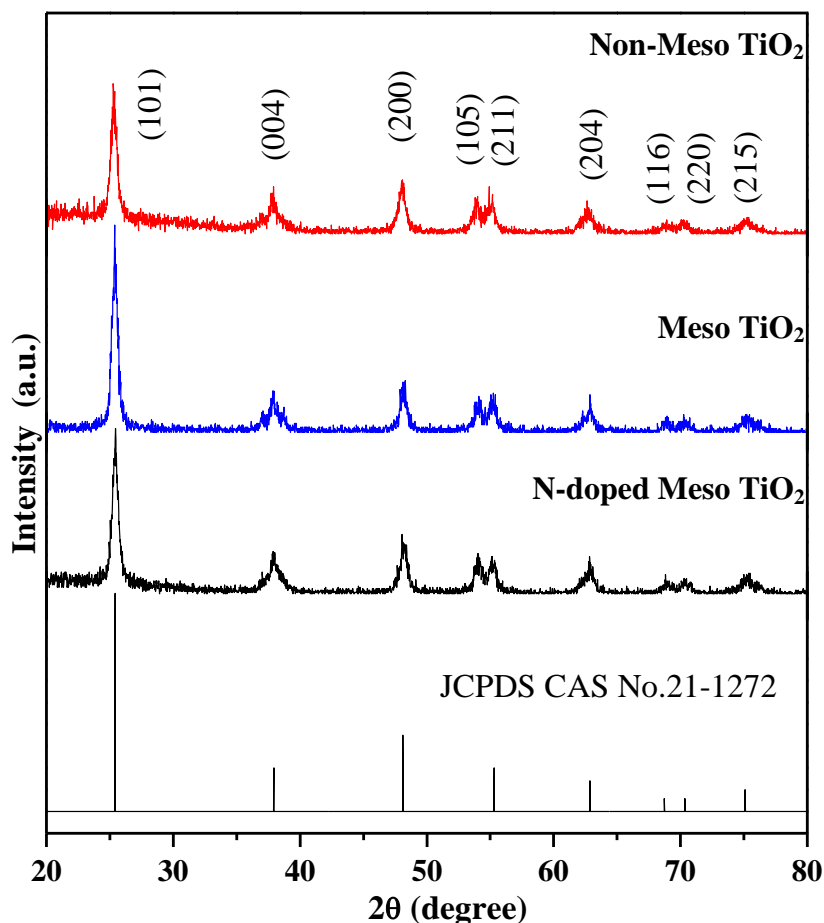
Figure 2. Large-angle powdered XRD patterns of various samples.

Table 1. Physical properties of various samples.

sample	S_{BET}[a] (m^2g^{-1})	D_{BJH}[b] (nm)	V_{tot}[c] (cm^3g^{-1})	d_p[d] (nm)
Non-Meso TiO_2	44	--	< 0.1	13.6
Meso TiO_2	55	9.4	0.1	17.2
N-doped Meso TiO_2	68	8.6	0.1	14.6

[a]BET surface area. [b]BJH pore diameter. [c]Total pore volume.
[d]Average crystallite size deduced by the Scherrer formula based on the (101) diffraction peak in Figure 2.

2p XPS spectra, characteristic of the Ti (IV) oxidation state. In particular, a broad Ti $2p_{3/2}$ feature of N-doped Meso TiO_2 samples containing two peaks suggested the existence of two different chemical environments of Ti ions which can be assigned to either an octahedral coordination with oxygen or a tetrahedral environment [43]. Moreover, a significant decrease in the binding energy of Ti $2p_{3/2}$ for N-doped Meso TiO_2 also implied that the substitution of a less electronegative nitrogen atom in the place of oxygen could happen, leading to a reduction of electron density around Ti. Accordingly, the N-doped Meso TiO_2 samples may possess moderate amount of N-doping in the TiO_2 framework, which is in line with the data in the XPS spectrum of N 1s (see Figure 5).
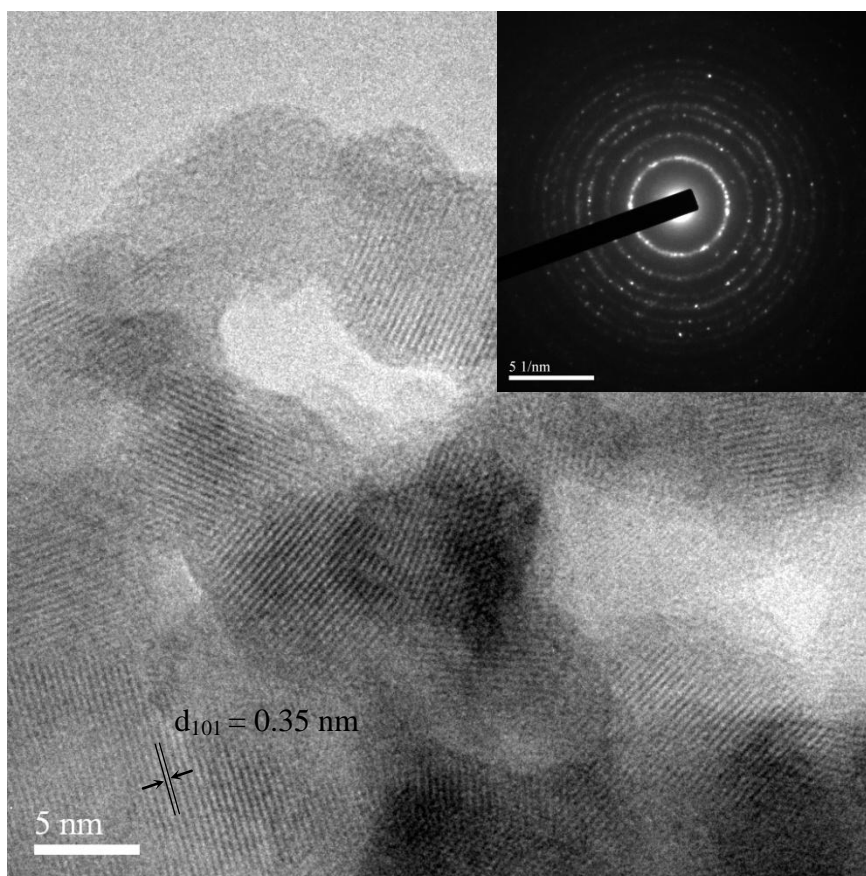

Figure 3. High magnification TEM image of N-doped Meso TiO_2 sample. Inset: the corresponding selected area electron diffraction pattern.

As shown in Figure 5, a broad peak centered at ca. 399.4 eV was observed in the N-doped Meso TiO_2 at N 1s region. This main peak can be deconvoluted into two peaks at 399.3 and 400.5 eV which are much higher than the typical binding energy of ≤ 397.5 eV observed for TiN [44], and lower than that of hyponitrite type nitrogen at 404 eV. The peaks of ≥ 400.3 eV could be attributed to molecular adsorbed nitrogen species. Nevertheless, the peaks located at binding energies of 397.5-400.3 eV, which might be ascribed to the N atom incorporating into the TiO_2 crystal lattice and substituting the oxygen atoms to form a O-Ti-N linkage [15,16]. It is noteworthy that the electron density around nitrogen is decreased and the binding energy of N1s in an O-Ti-N linkage is positively

shifted to a greater extent than that in an N-Ti-N linkage. Quantitatively, ca. 2.8 at% of nitrogen was successfully doped on N-doped Meso TiO$_2$ sample by analysis of XPS.
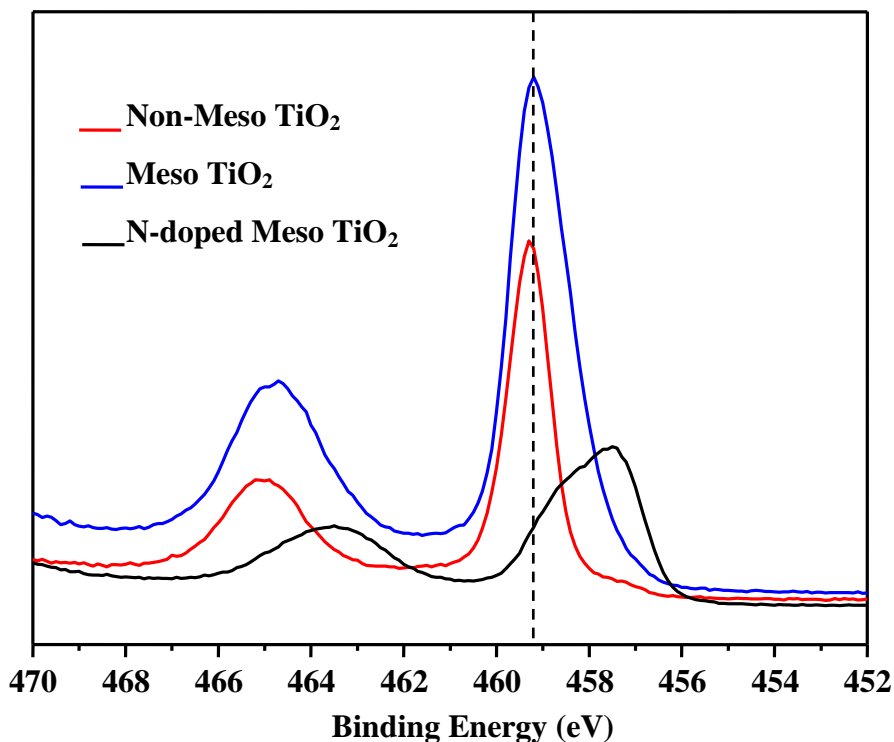

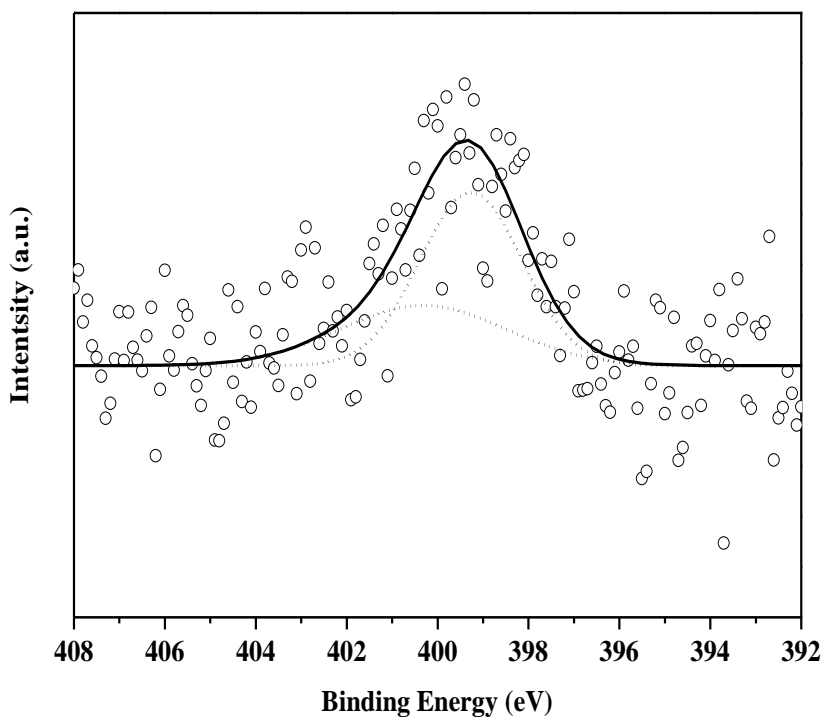**Figure 4.** XPS spectra of various samples at the Ti 2p region.

Figure 5. XPS spectrum of N-doped Meso TiO$_2$ sample at the N 1s region.

UV-visible diffuse reflectance spectrometry is the most common technique used to study the optical properties and examine the doping effects on the metal oxide matrix. As shown in Figure 6, it was found that Meso TiO_2 samples in the UV-visible absorption spectra possessed a red-shift absorbance threshold in comparison with Non-Meso TiO_2. The N-doped Meso TiO_2 samples presented a noticeable adsorption in the visible region between 400 and 500 nm, which is the typical adsorption feature of N-doped TiO_2, as compared with that of undoped Meso TiO_2 samples. It has been reported [45] that the existence of additional electronic states above the valence band edge could lead to the red-shift absorption of N-doped nanomaterials.
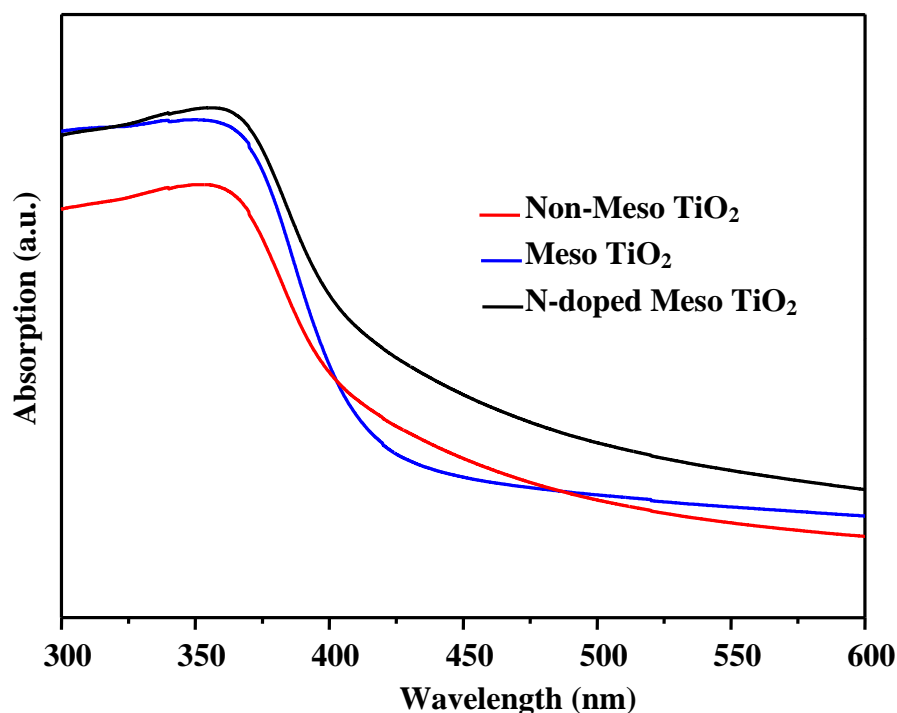

Figure 6. Diffuse reflectance UV-visible absorption spectra of various samples.

The photoelectrochemical performances of the DSSCs based on the Non-Meso TiO_2, Meso TiO_2 and N-doped Meso TiO_2 electrodes are shown in Figure 7 and Table 2. Among three solar cells, Non-Meso TiO_2 DSSCs achieved an energy conversion efficiency of 1.65%, V_{OC} (open circuit voltage) of 0.72 V, J_{SC} (short circuit current density) of 3.67 mA cm^{-2}, and *FF* (fill factor) of 63%. The poor energy conversion efficiency was mostly due to the low J_{SC}. The surface area of Non-Meso TiO_2 was ca. 44 m^2 g^{-1}, suggesting that the low J_{SC} was not mainly caused by the low surface area. Thus, it may be most likely due to the worst efficient electron collection from the network of TiO_2 to the FTO glass substrate. As can be seen in Table 2, the J_{SC} value of ca. 6.24 mA cm^{-2} in Meso TiO_2 was observed, which is almost double that of Non-Meso TiO_2. Thus, mesoporous TiO_2 have an unique hierarchical pore structure with continuous nanochannels between the primary particles and continuous external channels, which may render efficient electrolyte diffusions and enhance conversion efficiency [46]. In terms of *V*oc, the increase of *V*oc in N-doped Meso TiO_2 DSSCs should be attributed mostly to the doping of the nitrogen into the TiO_2 matrix, resulting in reduction of the charge recombination or

hindering the dark current [15]. Consequently, N-doped Meso TiO_2 DSSCs, due to its unique mesostructures and moderate N-doping in the TiO_2 framework, exhibited the optimal energy conversion efficiency (5.30%) among all prepared DSSCs.
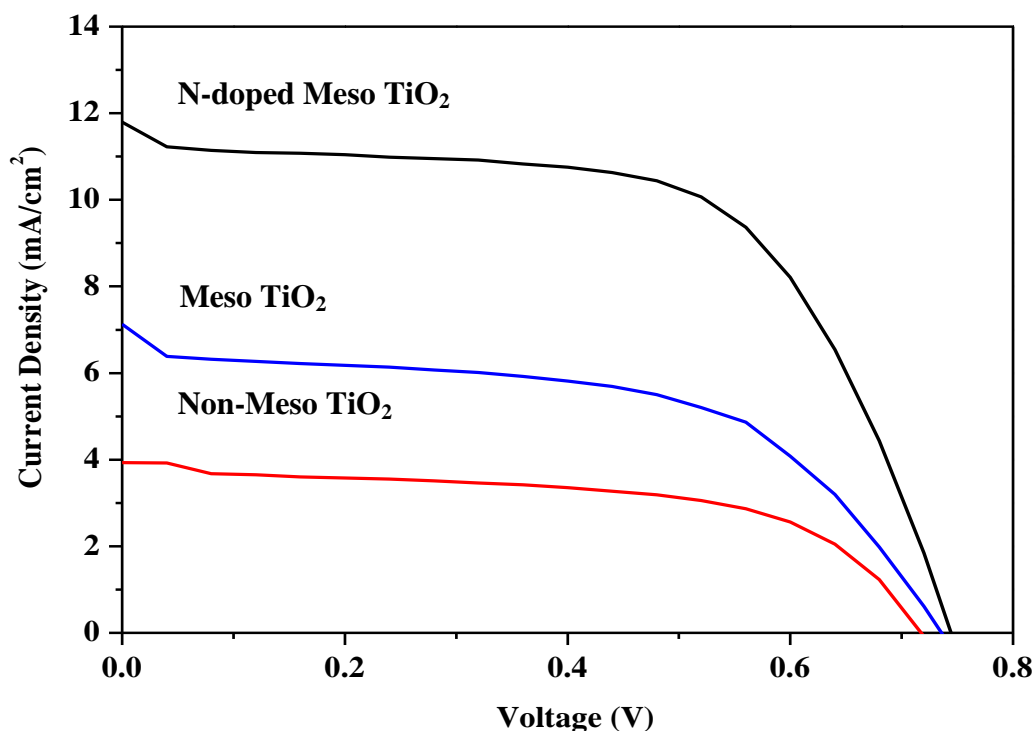

Figure 7. Photocurrent-voltage curves of the DSSCs based on the photoelectrodes prepared by various samples.

Table 2. Photovoltaic properties obtained from the photocurrent-voltage curves of DSSCs prepared by various photoelectrodes.

sample	V_{oc}[a] (V)	J_{sc}[b] (mA/cm^2)	FF[c]	η (%)
Non-Meso TiO_2	0.72	3.67	0.63	1.65
Meso TiO_2	0.73	6.24	0.63	2.84
N-doped Meso TiO_2	0.75	11.07	0.63	5.30

[a]Open circuit voltage. [b]Short circuit density. [c]Fill factor.

4. CONCLUSIONS

In conclusion, three TiO_2 and modified TiO_2 nanomaterials, namely Non-Meso TiO_2, Meso TiO_2, and N-doped Meso TiO_2, were fabricated by a simple EISA process. The resulting samples were characterized by a variety of various spectroscopic and analytical techniques and also used as photoanodes in the DSSCs. Compared to Non-Meso TiO_2 and Meso TiO_2, the N-doped Meso TiO_2

photoanode exhibited a surpassing photovoltaic performance, which possessed mesoporous structures with N-doping could successfully retard the charge recombination between TiO₂ photoelectrode and electrolyte interface and enhanced electron lifetime, which may be due to the fact that incorporation of nitrogen replaced the oxygen deficiency to form O-Ti-N in the titania crystal lattice. Thus, the N-doped Meso TiO₂ materials so fabricated should render future practical and cost-effective applications in solar-energy related areas, for instance, as photoanodes for DSSCs.

References

1. B.O. Regan and M. Gratzel, *Nature*, 353 (1991) 737-740.
2. R. Knodler, J. Sopka, F. Harbach, H.W. Grunling, *Sol. Energy Mater. Sol. Cells*, 30 (1993) 277-281.
3. G. Smestad, *Sol. Energy Mater. Sol. Cells*, 32 (1994) 273-288.
4. H. Pettersson, T. Gruszecki, *Sol. Energy Mater. Sol. Cells*, 70 (2001) 203-212.
5. D. Wei and G. Amaratunga, *Int. J. Electrochem. Sci.*, 2 (2007) 897-912.
6. A. Hagfeldt, G. Boschloo, L. Sun, L. Kloo, and H. Pettersson, *Chem. Rev.*, 110 (2010) 6595-6663.
7. V. Baglio, M. Girolamo, V. Antonucci, and A.S. Arico, *Int. J. Electrochem. Sci.*, 6 (2011) 3375-3384.
8. F. A. Nada, A. Galal, and H.M.A. Amin, *Int. J. Electrochem. Sci.*, 7 (2012) 3610-3626.
9. P. Teesetsopon, S. Kumar, and J. Dutta, *Int. J. Electrochem. Sci.*, 7 (2012) 4988-4999.
10. T. Bessho, E. Yoneda, J.H. Yum, M. Guglielmi, I. Tavernelli, H. Imai, U. Rothlisberger, M.K. Nazeeruddin, and M. Gratzel, *J. Am. Chem. Soc.*, 131, (2009) 5930-5934.
11. N.F. Atta, H.M.A. Amin, M.W. Khalil, and A. Galal, *Int. J. Electrochem. Sci.*, 6 (2011) 3316-3332.
12. J.J. Hill, N. Banks, K. Haller, M.E. Orazem, and K.J. Ziegler, *J. Am. Chem. Soc.*, 133, (2011) 18663-18672.
13. G. Sahu, K. Wang, S.W. Gordon, W.L. Zhou, and M.A. Tarr, *RSC Adv.*, 2 (2012) 3791-3800.
14. J. Du, J. Qi, D. Wang, and Z.Y. Tang, *Energy Environ. Sci.*, 5 (2012) 6914-6918.
15. H.J. Tian, L.H. Hu, C.N. Zhang, W.Q. Liu, Y. Huang, L. Mo, L. Guo, J. Sheng, and S.Y. Dai, *J. Phys. Chem. C*, 114 (2010) 1627-1632.
16. S.H. Kang, H.S. Kim, J.Y. Kim, and Y.E. Sung, *Mater. Chem. Phys.*, 124 (2010) 422-426.
17. W. Guo, L. Wu, Z. Chen, G. Boschloo, A. Hagfeldt, and T. Ma, *J. Photochem. Photobiol. A: Chem.*, 219 (2011) 180-187.
18. W. Guo, Y. Shen, L. Wu, Y. Gao, and T. Ma, *J. Phys. Chem. C*, 115 (2011) 21494-21499.
19. T.K. Yun, J.H. Cheon, J.Y. Bae, K.S. Ahn, and J.H. Kim, *J. Nanosci. Nanotech.*, 12 (2012) 3305-3308.
20. S. Rodrigues, K.T. Ranjit, S. Uma, I.N. Martyanov and K.J. Klabunde, *Adv. Mater.*, 17 (2005) 2467-2471.
21. S.-H. Liu and H.-R. Syu, *Applied Energy*, 100 (2012) 148-154.
22. R. Asahi, T. Morikawa, T. Ohwaki, K. Aoki, and Y. Taga, *Science*, 293 (2001) 269-271.
23. M. Maeda, T.J. Watanabe, *J. Electrochem. Soc.*, 153 (2006) C186-189.
24. M. Miyauchi, A. Ikezawa, H. Tobimatsu, H. Irie, K. Hashimoto, *Phys. Chem. Chem. Phys.*, 6 (2004) 865-870.
25. Y. Jun, J.H. Park, and M.G. Kang, *Chem. Commun.*, 48 (2012) 6456-6471.

26. S.-H. Liu, H.P. Wang, Y.-J. Huang, Y.M. Sun, K.-S. Lin, M.C. Hsiao and Y.S. Chen, *Energy Sources*, 25 (2003) 591-596.
27. M. Cabo, S. Garroni, E. Pellicer, C. Milanese, A. Girella, A. Marini, E. Rossinyol, S. Surinach, and M.D. Baro, *Int. J. Hydrogen Energy*, 36 (2011) 5400-5410.
28. S.-H. Liu and J.-R. Wu, *Int. J. Electrochem. Sci.*, 7 (2012) 8326-8336.
29. S.-H. Liu, W.-Y. Yu, C.-H. Chen, A.Y. Lo, B.-J. Hwang, S.-H. Chien and S.B. Liu, *Chem. Mater.*, 20 (2008) 1622-1628.
30. S.-H. Liu, F.S. Zheng and J.-R. Wu, *Appl. Catal. B Environ.*, 108-109 (2011) 81-89.
31. S.-H. Liu and J.-R. Wu, *Int. J. Hydrogen Energy*, 36 (2011) 87-93.
32. S.-H. Liu, Y.-C. Lin, Y.-C. Chien, and H.R. Hyu, *J. Air & Waste Manage. Assoc.*, 61 (2011) 226-233.
33. S.-H. Liu and S.-C. Chen, *Journal of Solid State Chemistry*, 184 (2011) 2420-2427.
34. S.-H. Liu and J.-R. Wu, *International Journal of Hydrogen Energy*, 37 (2012) 16994-17001.
35. S.K. Das, M.K. Bhunia, and A. Bhaumik, *Dalton Transactions*, 39 (2010) 4382-4390.
36. K. Sivaranjani and C.S. Gopinath, *J. Mater. Chem.*, 21 (2011) 2639-2647.
37. Z. Zhang, F. Zuo, and P. Feng, *J. Mater. Chem.*, 20 (2010) 2206-2212.
38. Y.-C. Lin, S.-H. Liu, H.-R. Syu, and T.-H. Ho, *Spectrochim. Acta A*, 95 (2012) 300-304.
39. T.S. Fong, M.R. Johan, and R.B. Ahmad, *Int. J. Electrochem. Sci.*, 7 (2012) 4716-4726.
40. W. G. Yang, F.R. Wan, Q.W. Chen, J.J. Li and D.S. Xu, *J. Mater. Chem.*, 20 (2010) 2870-2876.
41. C. Wu, T. Ohsuna, M. Kuwabara, and K. Kuroda, *J. Am. Chem. Soc.*, 128 (2006) 4544-4545.
42. W. Chae, S. Lee, and Y. Kim, *Chem. Mater.*, 17 (2005) 3072-3074.
43. G.S. Shao, F.Y. Wang, T.Z. Ren, Y. Liu, Z.Y. Yuan, *Appl. Catal. B Environ.*, 92 (2009) 61-67.
44. N.C. Saha, H.G. Tompkins, *J. Appl. Phys.*, 72 (1992) 3072-3079.
45. X. Chen and C. Burda, *J. Am. Chem. Soc.*, 130 (2008) 5018-5019.
46. Y. Zhao, X.L. Sheng, J. Zhai, L. Jiang, C.H. Yang, Z.W. Sun, Y.F. Li and D.B. Zhu, *ChemPhysChem*, 8 (2007) 856-861.